ACS OMEGA

http://pubs.acs.org/journal/acsodf

Article

Effects of a Multistage Fractured Horizontal Well on Stimulation Characteristics of a Clayey Silt Hydrate Reservoir

Junpeng Han, Xiaolong Ma,* and Dongbin Pan*

Cite This: *ACS Omega* 2022, 7, 35705−35719

Read Online

ACCESS | Metrics & More | Article Recommendations

ABSTRACT: The gas production from clayey silt natural gas hydrate (NGH) reservoir in the South China Sea faces the problem of low connectivity between the reservoir and the production well, which seriously reduces the gas production rate. Multistage fractured horizontal well (MFHW) is regarded as an effective technical means to improve gas production for an unconventional reservoir with low permeability. In this paper, a three-dimensional numerical simulation model was built to study the promotion effects of MFHW technology on gas production from a clayey silt NGH reservoir. The temporal and spatial evolution characteristics of the NGH reservoir with and without multiple fractures were compared and analyzed in detail. In addition, the influences of the fracture number, permeability, and morphology on the stimulation effect on gas production through MFHW technology were discussed. The results indicated that the fractures with high conductivity provided a fast channel for gas and water flow and increased the contact area between the horizontal well and the NGH reservoir, which had a positive effect on increasing gas production from the clayey silt NGH reservoir. Increasing fracture number, fracture permeability, and the area of fracture morphology effectively improved the gas production rate and total gas production, but the stage of the high gas production rate only lasted for a short time. This study demonstrated the production behavior of MFHW technology in the clayey silt NGH reservoir, which was helpful for understanding this technology's stimulation effect.

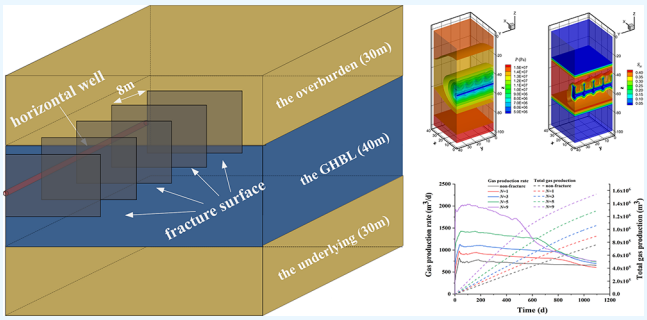

1. INTRODUCTION

Natural gas hydrate (NGH) is a new type of clean energy, which is widely distributed in terrestrial permafrost areas and marine sediments.[1,2] It is estimated that the resource of NGH is up to 3000 trillion cubic meters (TCM),[3] which is significantly higher than that of conventional gas (∼404 TCM) and shale gas (204−456 TCM).[4] Most NGH reservoirs occur in marine sediments, which are two orders of magnitude higher than those in terrestrial permafrost areas. At present, only China and Japan have carried out marine NGH production tests. Due to the low drilling cost and low technical difficulty, the depressurization method of a single vertical well was adopted in the first marine NGH production tests in Japan[5] and China.[6,7] However, based on varieties of numerical simulation works and marine NGH production tests, it is difficult to realize commercial NGH production through a depressurization method of the single vertical well. Therefore, how to improve gas production through a horizontal well;[8] the depressurization method combined with the thermal stimulation method,[9] multihorizontal[10] or vertical wells;[11] reservoir reconstruction;[12,13] or other technical means has become a research hotspot. Benefitting from the application of the horizontal well, the largest total gas production was realized in China's second marine production test.[14] However, due to the low permeability of clayey silt NGH reservoirs, there is still a big gap from commercial NGH production.

Reservoir stimulation technology can improve the permeability of NGH reservoirs near the production well, thereby increasing the depressurization effect and productivity, so it is regarded as a potential high-efficiency method. At present, the two marine NGH production tests in China effectively increased the gas production rate and total gas production through reservoir reconstruction.[6,14] However, the reservoir reconstruction area was limited to the periphery of production wells, which resulted in a lower gas production increase.[15] By constructing artificial channels with high conductivity, a multistage fractured horizontal well (MFHW) can effectively solve the low gas production problem caused by high flow resistance of low-permeability reservoirs, which is a potential technology for realizing commercial NGH production. MFHW technology has

Received: June 13, 2022
Accepted: September 15, 2022
Published: September 28, 2022

ACS Publications

© 2022 The Authors. Published by American Chemical Society

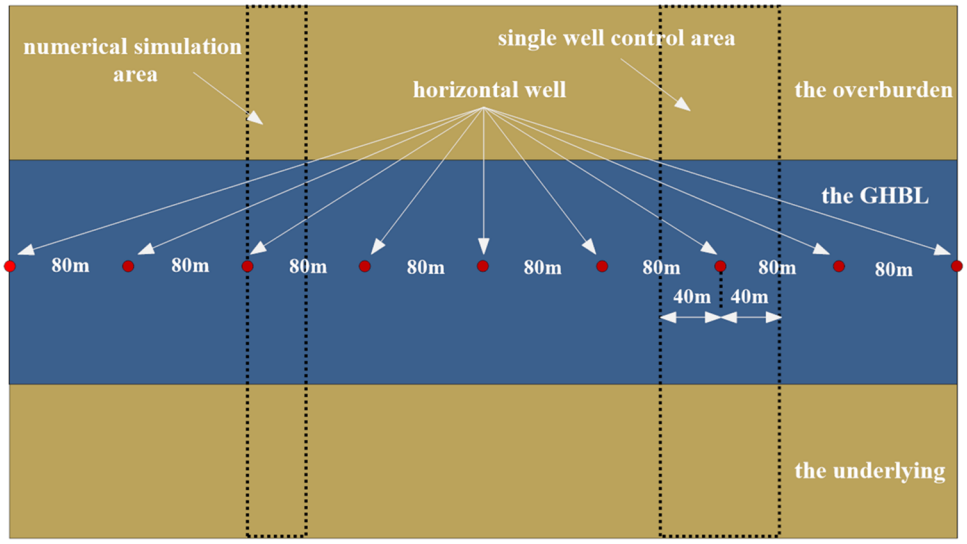

Figure 1. Schematic of the clayey silt NGH reservoir production by multihorizontal wells from top view.

been successfully applied to the commercial production of shale gas reservoirs, which greatly increases the gas production rate and total gas production. During the process of hydraulic fracturing in a shale reservoir, the complex fracture network with higher conductivity is mainly constructed by connecting natural fractures with hydraulic fractures. However, there are no natural fractures in the clayey silt NGH reservoir, so the stimulation process mainly depends on artificial fractures. The characteristics of hydraulic fracturing stimulation in shale gas reservoirs are obviously different from those in NGH reservoirs, so the relevant experience cannot be directly applied. At present, a large number of studies have been carried out on MFHW technology for shale, and a clear understanding of the fracture propagation law and the stimulation mechanism has been obtained.[16−23] However, MFHW technology for the NGH reservoir is still in its infancy. Only a few studies have investigated fracture propagation behavior and gas production characteristics, and no systematic conclusion has been formed.

In recent years, it has been proved by numerical simulation that the artificial fracture with high conductivity can increase the depressurization effect so that the hydrate decomposition gas can flow into the production well quickly and increase the gas production. Zhao et al.[24] built a core-scale numerical model to study the promotion effects of hydraulic fracture on gas production from hydrates, and the results indicated that the fracture effectively enhanced the depressurization range through an additional flow channel. Ma et al.[25] investigated the influence of the horizontal well location and the fracture length on gas production and found that the gas flowing through the fracture to the production well accounted for a large part of the total gas production. Feng et al.[26] compared the stimulation effect of fractures on NGH reservoirs with high temperature and low temperature and found that NGH reservoirs with high temperature were more conducive to reservoir transformation. However, in the previous studies on hydraulic fracturing stimulation of horizontal wells, the fractures were usually set as the high conductivity area along the direction of horizontal wells, and few studies set the fractures perpendicular to horizontal wells.

In this study, a three-dimensional MFHW numerical model was built to study the promotion effect of multiple fractures on gas production from the clayey silt NGH reservoir. The spatial characteristic parameters such as temperature, pressure, hydrate saturation, and gas saturation through MFHW technology were studied in detail. Meanwhile, the influence of the fracture number, permeability, and morphology on gas and water production was discussed.

2. CONSTRUCTION OF THE NUMERICAL SIMULATION MODEL

2.1. Numerical Simulation Software. In this study, tough + hydrate, which was developed by the Lawrence Berkeley National Laboratory, was used to simulate the nonisothermal gas release, phase transformation, and heat and fluid flow during hydrate formation and decomposition in the hydrate-bearing sediments with different scales.[27,28] By solving coupled equations of mass and heat balance, this software can simulate gas production from the NGH reservoir in permafrost and marine sediments, which is regarded as the most useful hydrate productivity simulation software. The accuracy of this software for hydrate formation and decomposition has been proved through laboratory experiments[29−31] and the production test.[7,32,33]

2.2. Numerical Simulation Model of MFHW. Compared with vertical wells, the length of horizontal wells passing through the NGH reservoir is large, which increases the contact area between the production well and NGH reservoirs, thereby increasing the gas production of the single well and reducing the production cost. Figure 1 shows the schematic of the clayey silt NGH reservoir production by multihorizontal wells from top view, wherein the red dots are the radial section of the horizontal well. As shown in Figure 1, it is assumed that the NGH reservoir in the South China Sea is exploited by the horizontal well group. Each horizontal well is located at the same depth of the NGH reservoir, and the trajectory direction of the production well is consistent. The well spacing between adjacent horizontal wells is 80 m, that is, the controllable production area is 40 m on both sides of the production well when using the same depressurization production scheme on horizontal wells. The control area is symmetrical about the horizontal well, making the symmetry plane an adiabatic and nonmass transfer boundary. Therefore, to simplify the numerical simulation model and improve the calculation speed, the simulation area shown in the black dotted box is taken as the research object.[34]

https://doi.org/10.1021/acsomega.2c03667
ACS Omega 2022, 7, 35705−35719

Figure 2 shows the schematic of MFHW simulation for a clayey silt NGH reservoir. The fractures are vertical, which are perpendicular to the axis of the horizontal well. In this paper, the direction of the first principal stress (maximum principal stress) is vertical, and the second and third principal stresses have the same value and are along the horizontal direction. Since hydraulic fractures generally propagate along the vertical direction of the minimum principal stress, it is easy to form multiple fracture surfaces perpendicular to the horizontal wellbore axis when using MFHW technology. The simulation of different fracture spacings can be realized by setting different numbers of fractures within the length range of a 40 m horizontal well. The number and spacing of fractures in Figure 2 are 5 and 8 m, respectively.

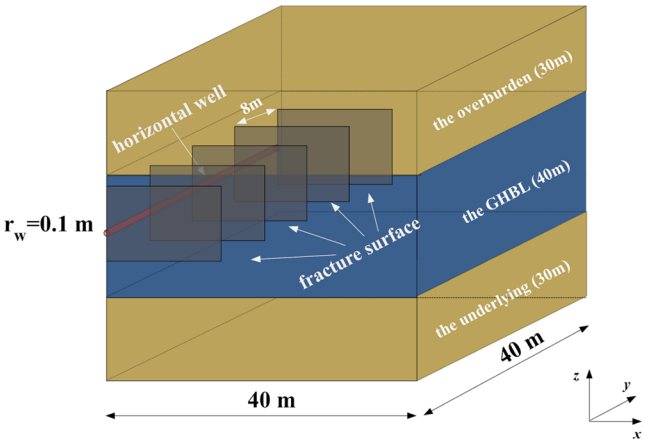

Figure 2. Schematic of MFHW stimulation for the clayey silt NGH reservoir.

In previous work, the cohesive element method was used to study the fracture morphology under different fracturing fluid injection rates.[35] In this work, the fracture morphology was extracted to build a three-dimensional MFHW numerical model. As shown in Figure 3a, the length and the height of the fracture were 5 and 10 m, respectively, which were produced at an injection rate of 0.005 m^3/s. As shown in Figure 3b, the length and the height of the fracture were 5 and 16 m, respectively, which were produced at an injection rate of 0.01 m^3/s. As shown in Figure 3c, the fracture morphology was not a regular rectangle, and the maximum length and height were 10 and 16 m, respectively, which were produced at an injection rate of 0.02 m^3/s.

Figure 4 shows the mesh diagram of MFHW stimulation for a clayey silt NGH reservoir. The model dimensions in the x, y, and z directions are 40, 40, and 100 m, respectively. The y-direction is the axis direction of the horizontal well, and the z-direction is the gravity direction. According to the properties of the NGH reservoir in the SH2 site, the thickness of the gas hydrate-bearing layer (GHBL) is set to 40 m, and the thickness of the overburden

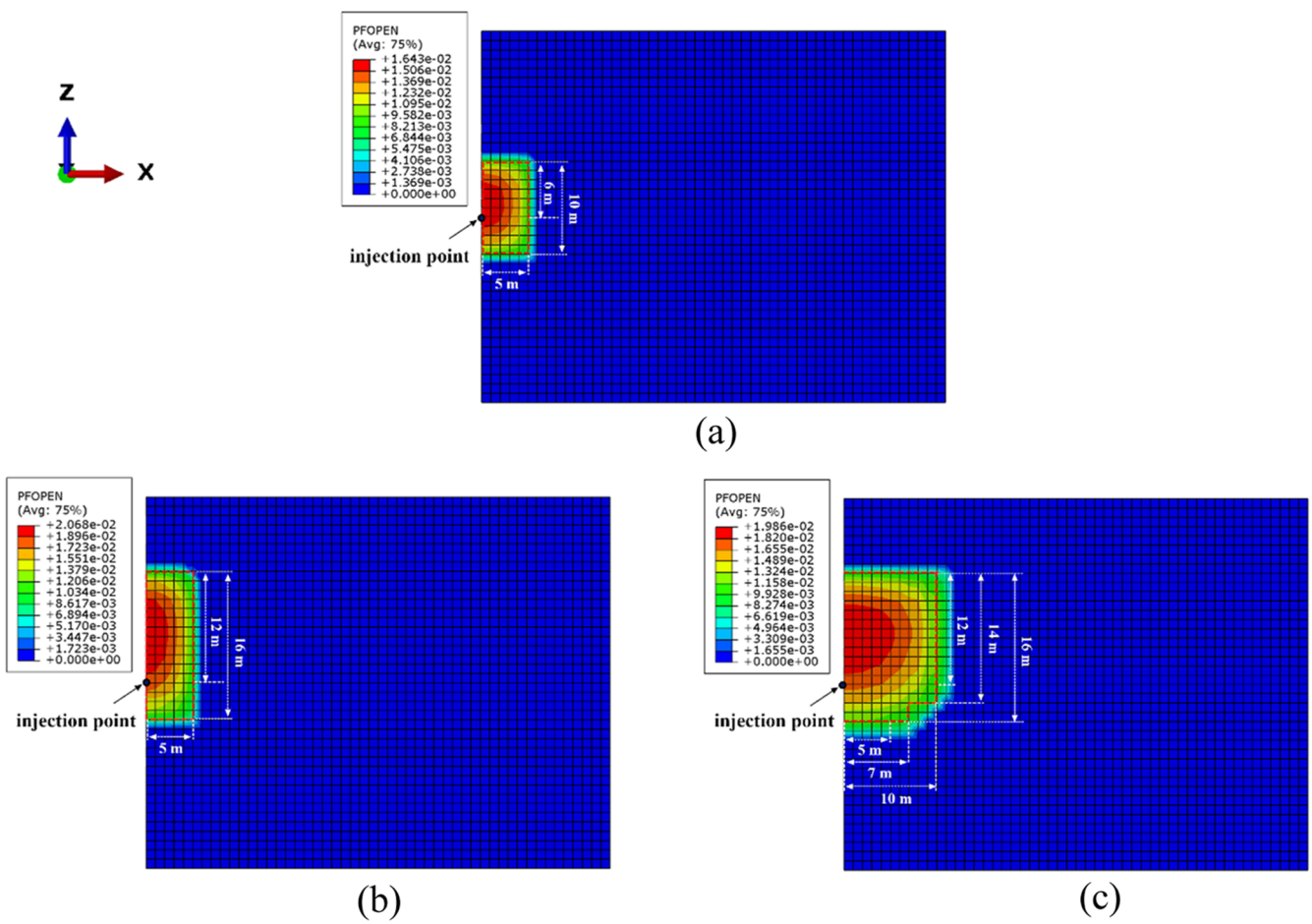

Figure 3. Extraction of fracture morphology under three different fracturing fluid injection rates: (a) $Q = 0.005\ m^3/s$, (b) $Q = 0.01\ m^3/s$, and (c) $Q = 0.02\ m^3/s$.

https://doi.org/10.1021/acsomega.2c03667
ACS Omega 2022, 7, 35705−35719

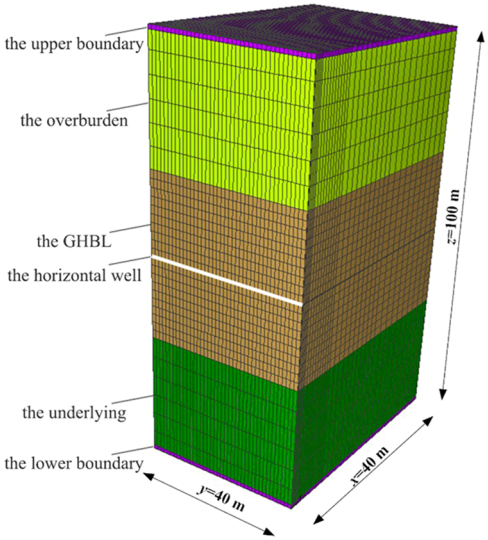

Figure 4. Mesh diagram of MFHW stimulation for the clayey silt NGH reservoir.

and underlying layer is set to 30 m, respectively. The upper and the lower boundaries are set as constant temperature and pressure conditions for fluid and heat exchange. The overburden and underlying layer with a thickness of 30 m are sufficient to accurately simulate the heat and mass exchange during 3 years of production.[36] In the MFHW technology of shale gas reservoirs, the length of the horizontal well can reach thousands of meters.[37] Assuming that the reservoir properties in the *y*-direction are consistent,[38] only a part of the horizontal well with a 40 m length is taken for research. The radius of the horizontal production well is set to 0.1 m. In the *x*-direction, the meshes in the region close to the production well are finer to accurately obtain the change characteristics of temperature, pressure, and hydrate saturation caused by rapid hydrate decomposition.[39] The mesh size in the *y*-direction is uniformly set to 1 m. In the *z*-direction, the mesh size of the upper and lower boundary is 1 m, and the mesh thickness of the overburden and the underlying layer is 4 m (1 layer) and 5 m (4 layers). The mesh thickness of the horizontal well, GHBL adjacent to the horizontal well, and other GHBL is 0.2, 1.9, and 2 m, respectively. When there are vertical fractures in the model, the fracture mesh is inserted in the corresponding position. The vertical fractures are simulated by inserting thin meshes at the preset location.

2.3. Initial and Boundary Conditions. The temperature at the bottom of the GHBL is set to 14.87 °C,[33,40,41] and the geothermal gradient is set to 4.7 °C/100 m[33,40,41] to calculate the initial temperature distribution of the model. Since the overburden, GHBL, and underlying are considered permeable, the pressure distribution of the model can be calculated by the hydrostatic pressure formula. Both the upper and lower boundaries of the model are set to constant temperature and pressure to allow fluid transfer and heat exchange. Due to the symmetry of the model, there is no fluid flow and heat exchange at the side boundary of the model.[42,43] Therefore, the side boundary is set as a Neumann boundary condition with no flux.

The thickness of the overburden and underlying layers is set to 30 m to meet the transfer of heat and pressure during long-term production,[34,44,45] and the thickness of GHBL is set to 40 m. The porosity of the overburden and underlying layers is 38%,[46] and the pores are filled with seawater with a salinity of 3.05%. The porosity of the GHBL is consistent with that of the overburden and underlying. Nearly 40% of the pore space is occupied by hydrate in the GHBL, and the remaining space is occupied by seawater with a salinity of 3.05%. The intrinsic permeability of the overburden, GHBL, and underlying is similar, which are set to 10 mD.[46] The sediment particle density is 2600 kg/m^3, and the thermal conductivity of dry and saturated sediments is 1.0 and 3.1 W/(m·°C), respectively.

The relative permeability of gas and water refers to the ratio of the effective permeability to the intrinsic permeability. Since hydrates exist in the form of solid phases in the pore space of sediments, their relative permeability is regarded as zero. The

Table 1. Main Parameters of the Numerical Simulation Model

parameter	value	parameter	value
thickness of overburden	30 m	relative permeability	$k_{rw} = \left(\frac{S_w - S_{irw}}{1 - S_{irw}}\right)^n$ $K_{rg} = \left(\frac{S_g - S_{irg}}{1 - S_{irw}}\right)^{n_g}$
thickness of underlying	30 m	water relative permeability index of the reservoir	4.5
thickness of GHBL	40 m	gas relative permeability index of the reservoir	3.5
horizontal well length	40 m	irreducible water saturation of the reservoir	0.30
production well radius	0.1 m	irreducible gas saturation of the reservoir	0.03
pressure of GHBL's bottom	14.97 MPa	water relative permeability index of fracture	3.5
temperature of GHBL's bottom	14.87 °C	gas relative permeability index of fracture	2.5
gas composition	100% CH_4	irreducible water saturation of fracture	0.20
porosity	38%	irreducible gas saturation of fracture	0.02
initial saturation of GHBL	$S_w = 0.60$, $S_H = 0.40$	capillary pressure	$P_{cap} = -P_0[(S^*)^{-1/\lambda} - 1]^{1-\lambda}$ $S^* = \frac{S_w - S_{irw}}{S_{mxw} - S_{irw}}$
intrinsic permeability	10 mD	pore structure index	0.45
pore water salinity	3.05%	gas entry pressure of the reservoir	1×10^5 Pa
particle density	2600 kg/m^3	gas entry pressure of fracture	1×10^4 Pa
thermal conductivity of dry sediments	1.0 W/m/K	maximum capillary pressure	1×10^6 Pa
thermal conductivity of water-saturated sediments	3.1 W/m/K	pore compressibility coefficient	1.0×10^{-8} Pa^{-1}

https://doi.org/10.1021/acsomega.2c03667
ACS Omega 2022, 7, 35705−35719

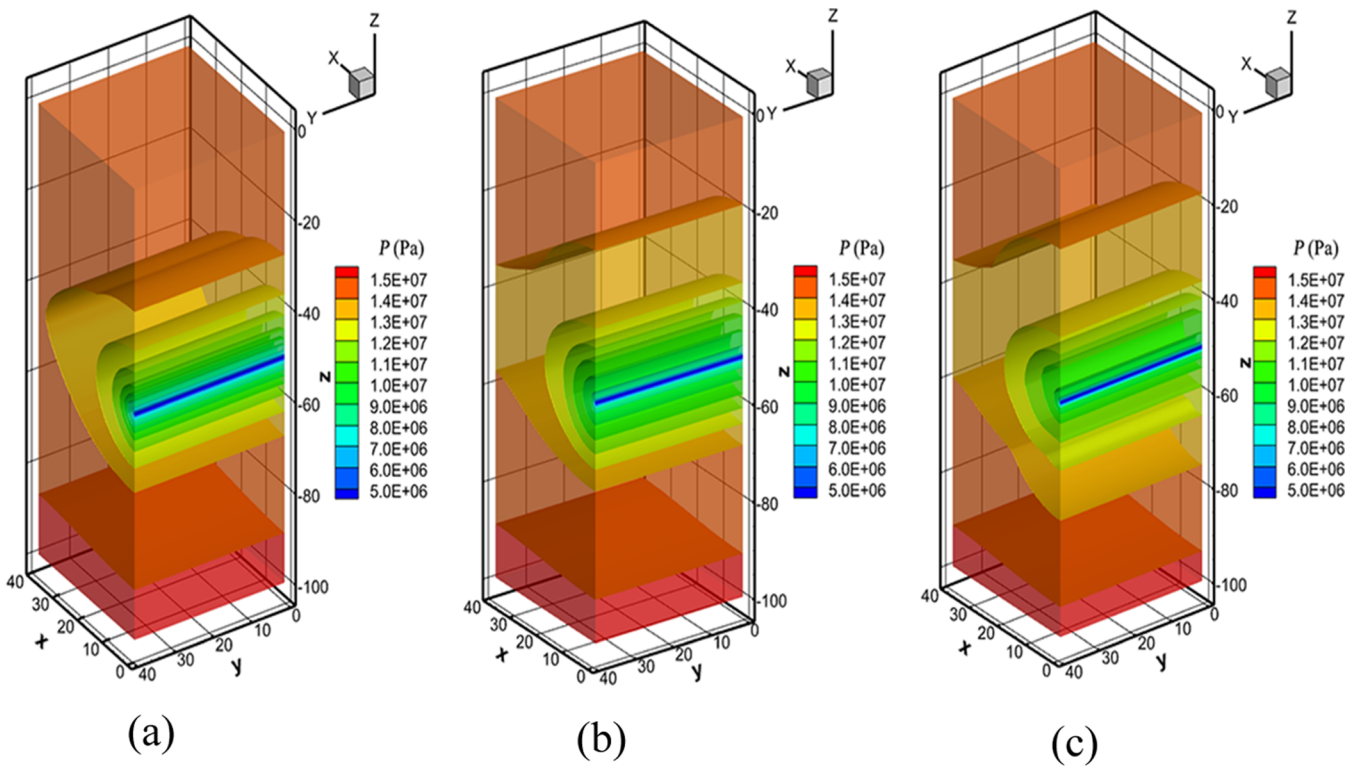

Figure 5. Spatial distribution characteristics of pore pressure in the NGH reservoir without MFHW at (a) 60 days, (b) 365 days, and (c) 1095 days.

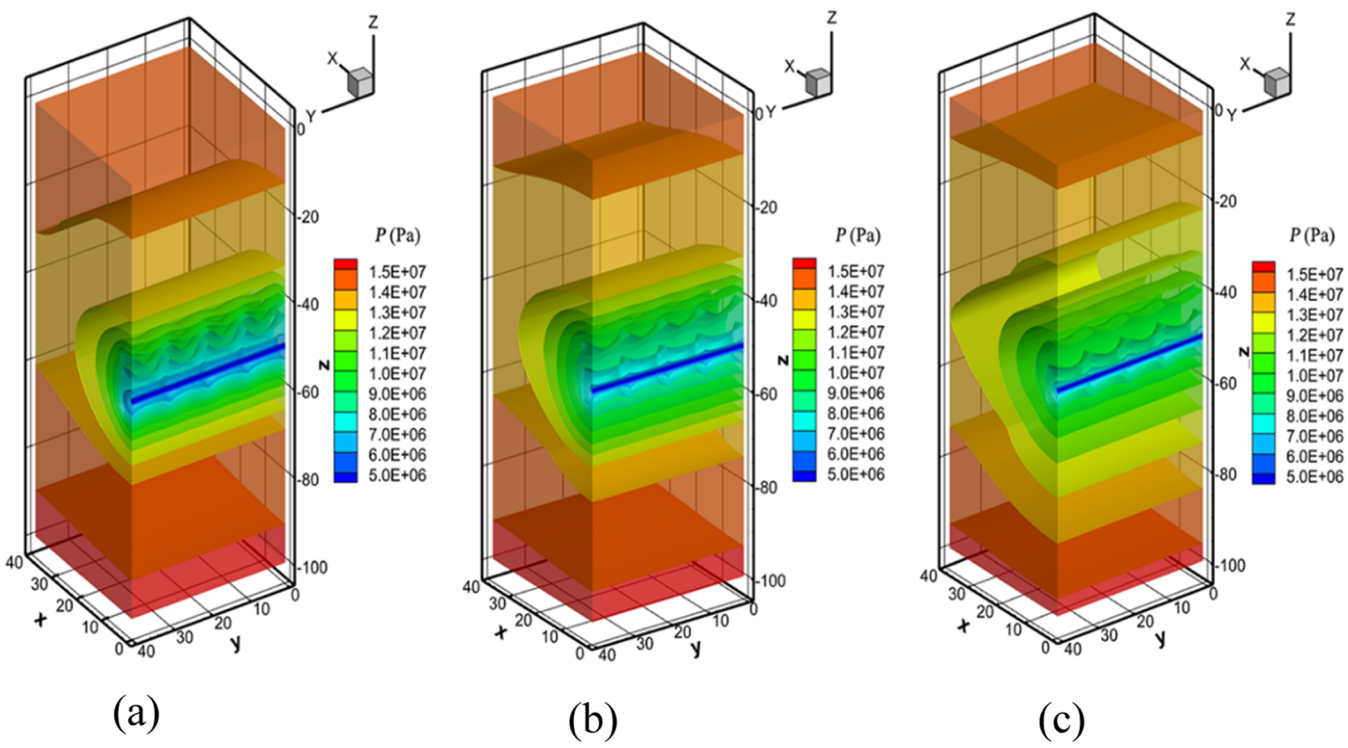

Figure 6. Spatial distribution characteristics of pore pressure in the NGH reservoir with five vertical fractures at (a) 60 days, (b) 365 days, and (c) 1095 days.

relative permeability of water (K_{rw}) and gas (K_{rg}) can be calculated by Stone's model[27] as follows

$$K_{rw} = \left(\frac{S_w - S_{irw}}{1 - S_{irw}}\right)^n \tag{1}$$

$$K_{rg} = \left(\frac{S_g - S_{irg}}{1 - S_{irw}}\right)^{n_g} \tag{2}$$

where S_w and S_g are water and gas saturation, respectively, and their values are between 0 and 1. S_{irw} and S_{irg} are irreducible

https://doi.org/10.1021/acsomega.2c03667
ACS Omega 2022, 7, 35705−35719

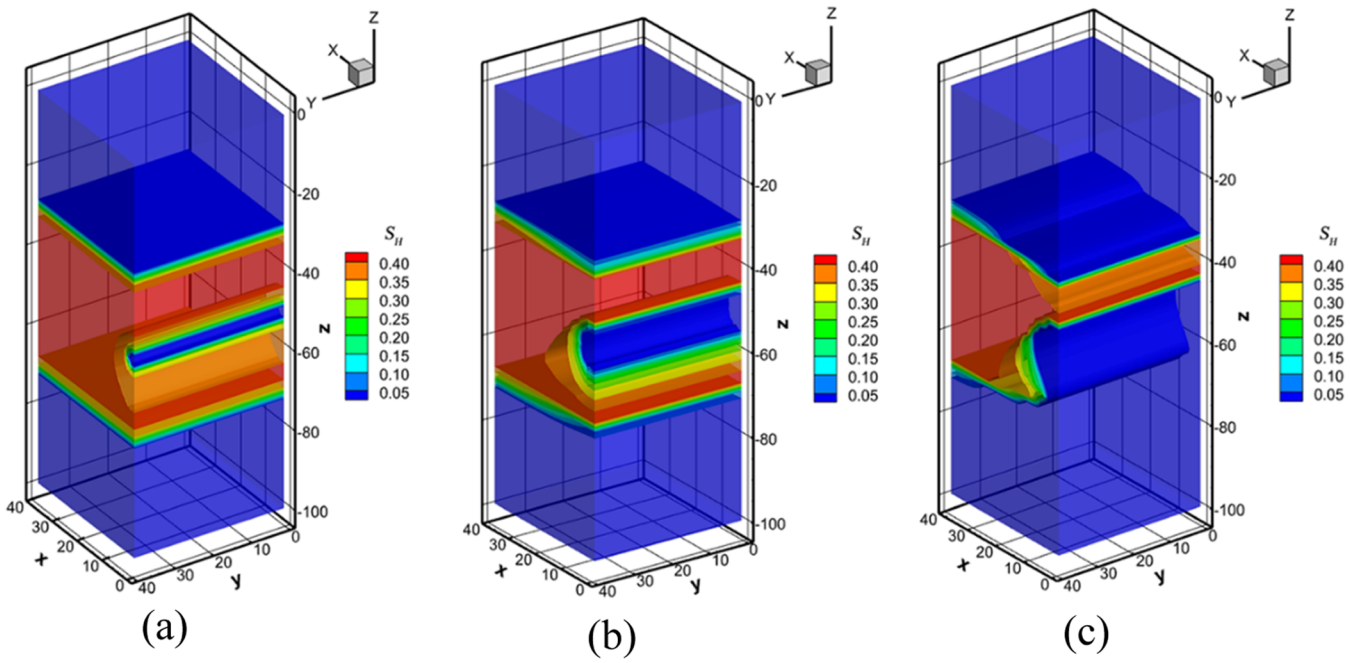

Figure 7. Spatial distribution characteristics of hydrate saturation in the NGH reservoir without MFHW at (a) 60 days, (b) 365 days, and (c) 1095 days.

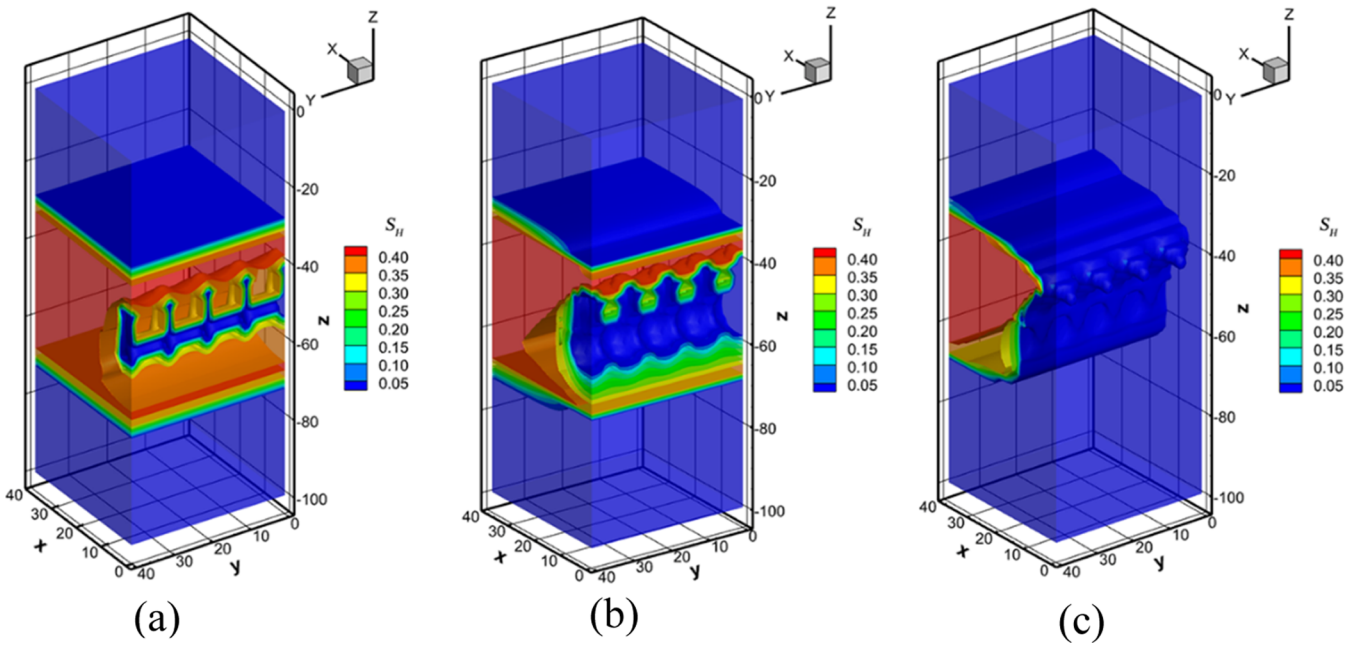

Figure 8. Spatial distribution characteristics of hydrate saturation in the NGH reservoir with five vertical fractures at (a) 60 days, (b) 365 days, and (c) 1095 days.

water and gas saturation, which are set to 0.30 and 0.03 for the NGH reservoir[40,41] and 0.20 and 0.02 for fracture, respectively. The water relative permeability (n) and gas relative permeability (n_g) of the NGH reservoir are 4.5 and 3.5, respectively.[15] The n and n_g of hydraulic fracture are 3.5 and 2.5, respectively.

When multiphase fluids such as gas and water exist in the pore space of NGH reservoirs, not only the relative permeability changes but also the surface tension effect between different phases leads to the generation of capillary pressure.[27] According to the van Genuchten model, the capillary pressure P_{cap} can be calculated by the following equations

$$P_{cap} = -P_0[(S^*)^{-1/\lambda} - 1]^{1-\lambda} \tag{3}$$

$$S^* = \frac{S_w - S_{irw}}{S_{mxw} - S_{irw}} \tag{4}$$

$$-P_{max} \leq P_{cap} \leq 0 \tag{5}$$

where P_0 is the gas entry pressure, with a value of 1×10^5 Pa for the NGH reservoir and 1×10^4 Pa for fracture; λ is the pore structure index, with a value of 0.45; S^* and S_{mxw} are proportional saturation and maximum water saturation; and

https://doi.org/10.1021/acsomega.2c03667
ACS Omega 2022, 7, 35705−35719

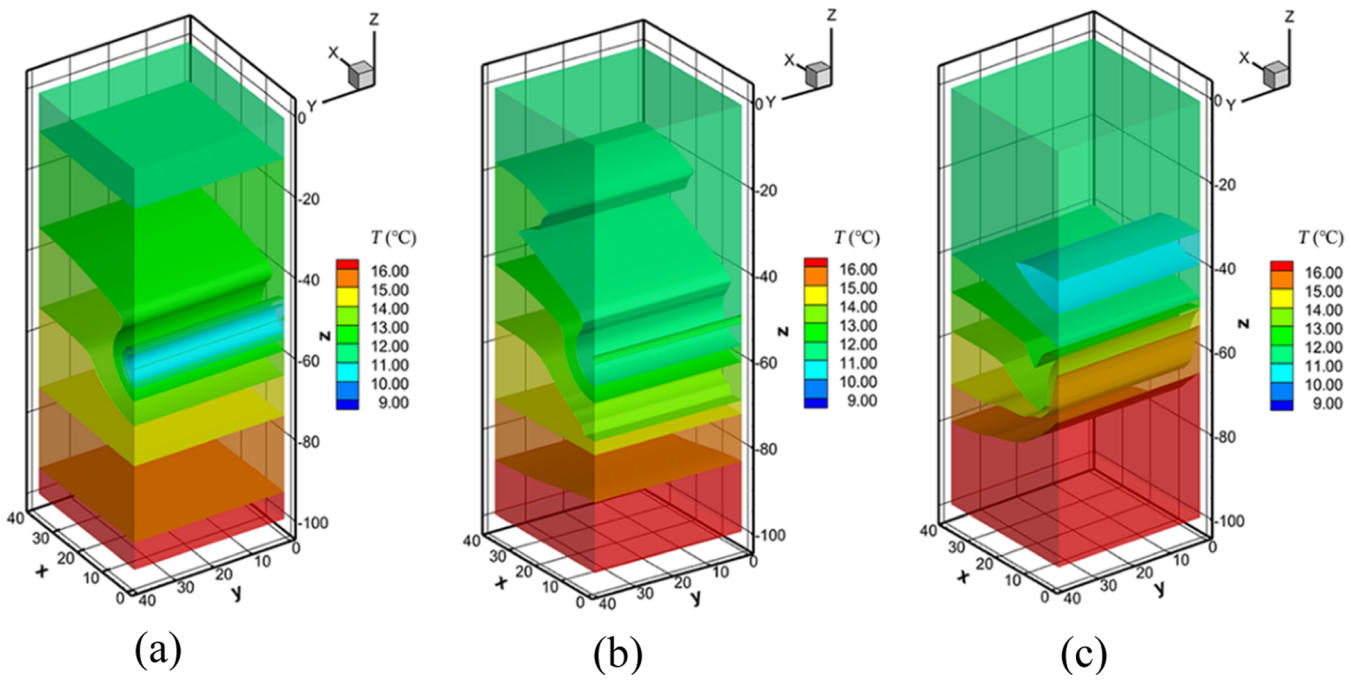

Figure 9. Spatial distribution characteristics of temperature in the NGH reservoir without MFHW at (a) 60 days, (b) 365 days, and (c) 1095 days.

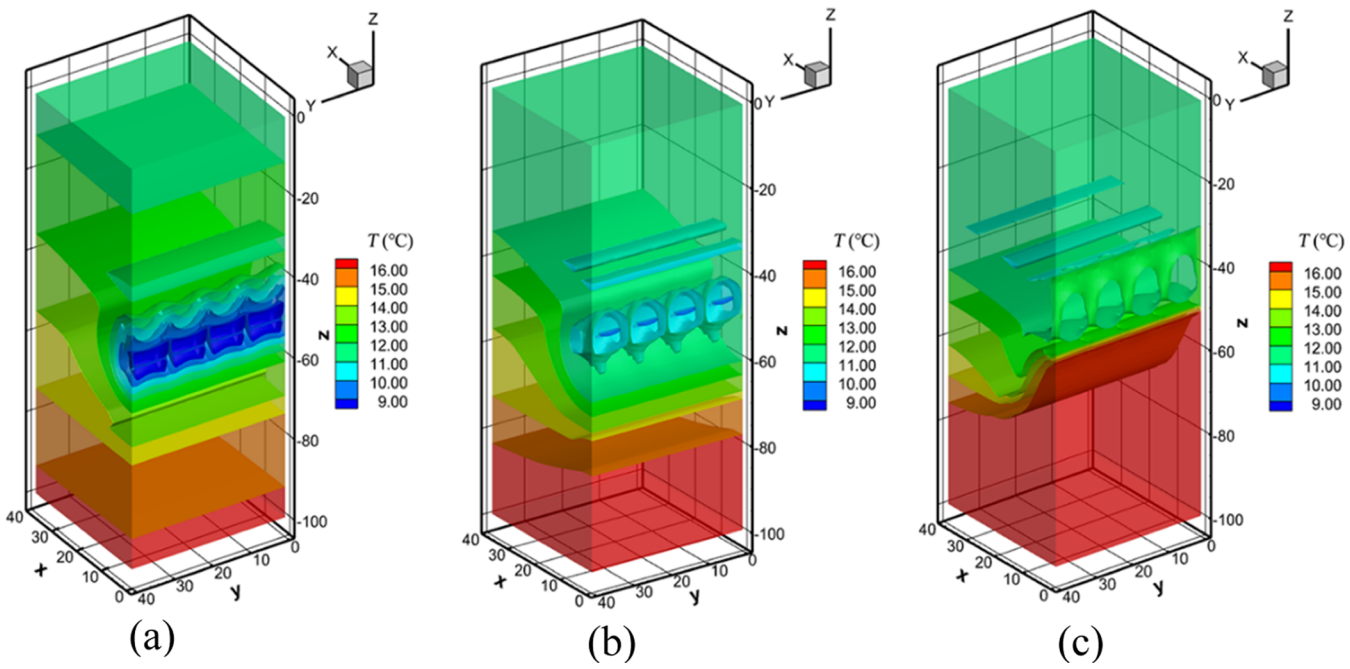

Figure 10. Spatial distribution characteristics of temperature in the NGH reservoir with five vertical fractures at (a) 60 days, (b) 365 days, and (c) 1095 days.

P_{max} is the maximum capillary pressure, which is set to 1×10^6 Pa.

The horizontal well is regarded as a pseudo porous medium with high permeability and porosity, which are set to 1×10^6 D and 99.9%, respectively. The capillary pressure in the production well is 0, and the irreducible water and gas saturation are set to a minimum value of 0.002 and 0.001, respectively. The depressurization production process lasts for 3 years. The main parameters of the numerical simulation model are shown in Table 1.

3. EVALUATION OF THE MULTIFRACTURE STIMULATION EFFECT

3.1. Spatial Distribution Characteristics of Reservoir Parameters. Figure 5 shows the spatial distribution characteristics of pore pressure in the NGH reservoir without MFHW at different times. As shown in Figure 5, the depressurization effects of the horizontal well cause the pore pressure in the NGH reservoir to decrease continuously, and the depressurization range shows an expanding trend as production continues. However, compared with the 365th day, the range of the low-pressure area (<8 MPa) on the 1095th day is significantly

https://doi.org/10.1021/acsomega.2c03667
ACS Omega 2022, 7, 35705−35719

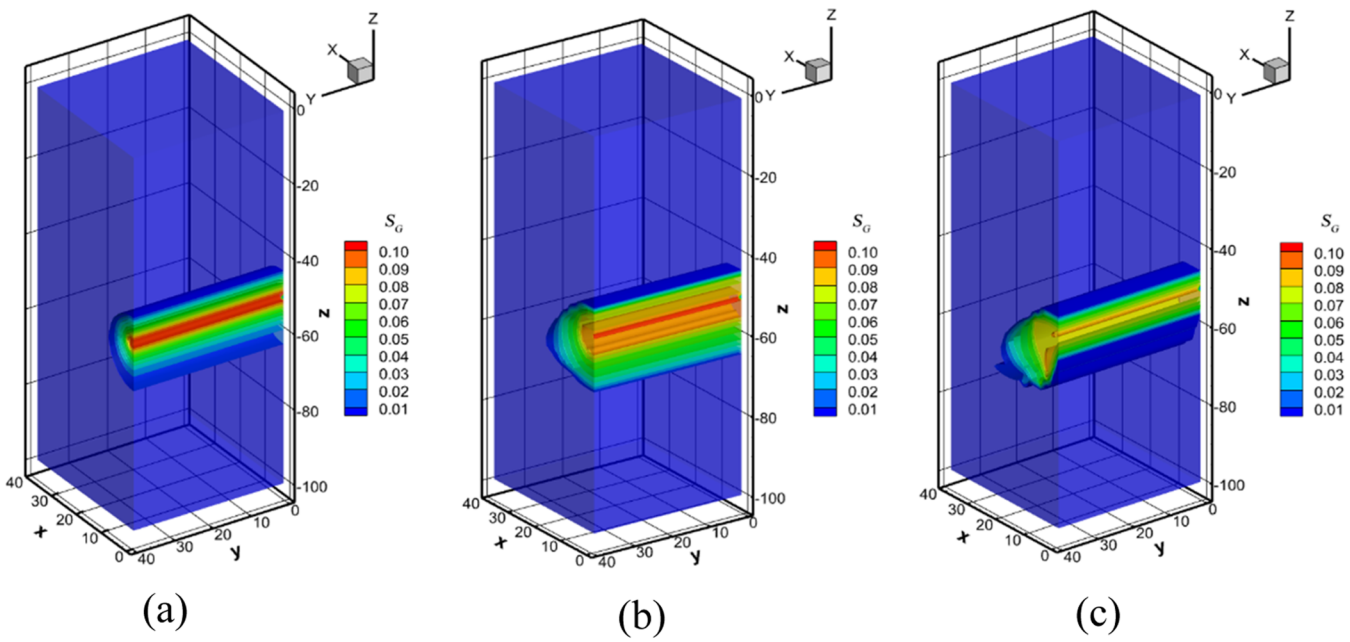

Figure 11. Spatial distribution characteristics of gas saturation in the NGH reservoir without MFHW at (a) 60 days, (b) 365 days, and (c) 1095 days.

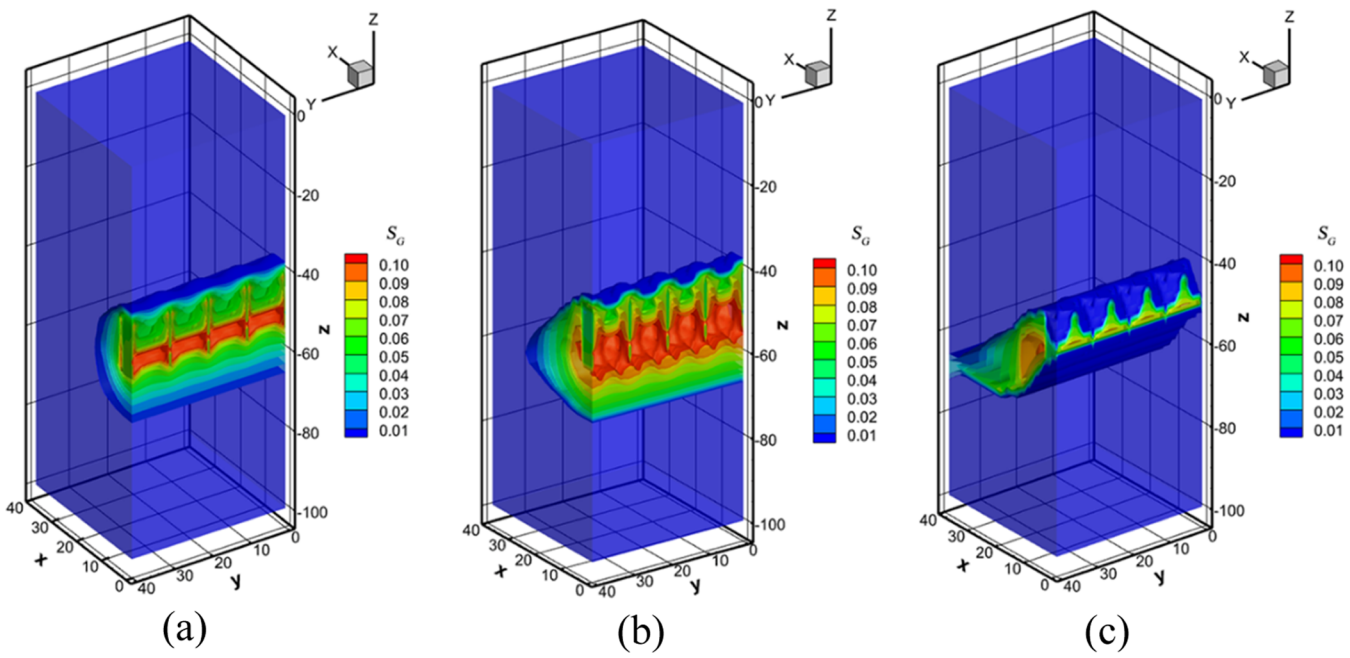

Figure 12. Spatial distribution characteristics of temperature in the NGH reservoir with five vertical fractures at (a) 60 days, (b) 365 days, and (c) 1095 days.

reduced. This is due to the rapid increase in the water production rate, which inhibits the depressurization effect in the near-well area. Figure 6 shows the spatial distribution characteristics of pore pressure in the NGH reservoir with five vertical fractures at different times. The presence of vertical fractures with high conductivity makes the front edge of depressurization in the NGH reservoir show obvious inhomogeneous features, and the depressurization effect in the near-field region of fractures is significantly stronger than that in the far-field region of fractures. Since the conductivity of fractures far exceeds the natural flow capacity of NGH reservoirs, the gas and water generated by hydrate decomposition near the fractures and the original pore water in the NGH reservoir preferentially flow into the production wells through the high conductivity fractures, reducing the flow resistance and enhancing the depressurization effect.

Figure 7 shows the spatial distribution characteristics of hydrate saturation in the NGH reservoir without MFHW at different times. As shown in Figure 7, the front edge of hydrate decomposition continues to expand outward along the radial direction of the horizontal well. It is obvious that the hydrate decomposition rate of the NGH reservoir in the lower part of the horizontal well is higher than that in the upper part, which is because the lower part can provide more heat for hydrate decomposition. On 60th and 365th days, the undecomposed zone of hydrates in the upper and lower parts of the horizontal well

https://doi.org/10.1021/acsomega.2c03667
ACS Omega 2022, 7, 35705−35719

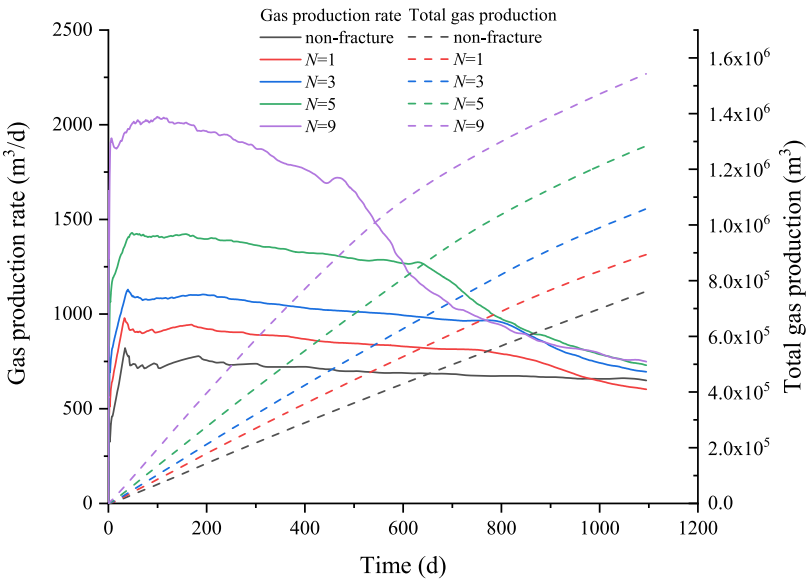

Figure 13. Evolution of the gas production rate and total gas production with time under different fracture numbers.

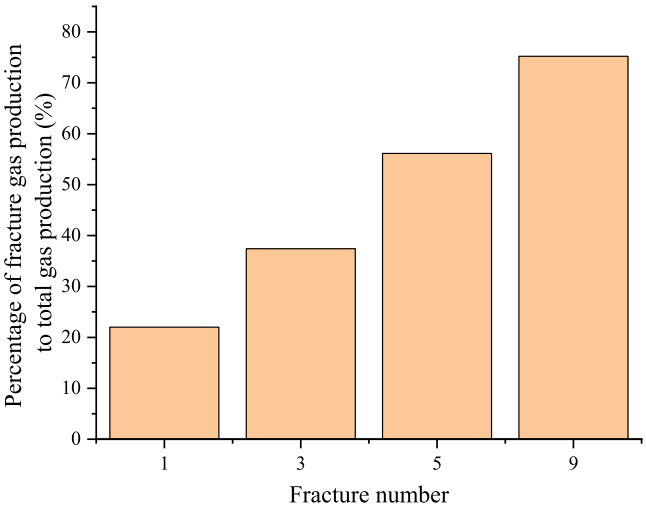

Figure 14. Percentage of gas production from fracture to total gas production under different fracture numbers.

acts as a low-permeability barrier to prevent warmer water from flowing into the horizontal well. On the 1095th day, the complete decomposition of hydrates in the lower part of the horizontal well weakens its water-blocking barrier, resulting in an increase in water production, which limits the low-pressure area, as shown in Figure 5. Figure 8 shows spatial distribution characteristics of hydrate saturation in the NGH reservoir with five vertical fractures at different times. As shown in Figure 8a,b, compared with the unfractured case, the vertical fractures with high conductivity change the front edge of hydrate decomposition from a single radial distribution pattern to a distribution pattern in which radial and fracture propagation directions coexist. As shown in Figure 8c, the hydrates at the upper and lower parts of the horizontal well at 1095 days are completely decomposed so that the function of the water-blocking barrier with low permeability is lost, which directly leads to a rapid decline in the gas production rate and a rapid increase in the water production rate in the later stage of production.

Figure 9 shows spatial distribution characteristics of temperature in the NGH reservoir without MFHW at different times. The hydrate decomposition reaction is an endothermic reaction, which leads to a decrease in reservoir temperature. On the 60th day, since the front edge of the hydrate decomposition gradually expands radially outward from the horizontal well, the low-temperature area is mainly distributed around the horizontal well. On the 365th and 1095th day, the low-temperature region around the horizontal well gradually disappears with the continued expansion of the decomposition front and the heat supplement of the surrounding strata. Figure 10 shows spatial distribution characteristics of temperature in the NGH reservoir with five vertical fractures at different times. On the 60th day, the temperature drop around the horizontal well in the fractured case is more obvious than that in the unfractured case. On the one hand, fractures enhance the depressurization effect of horizontal wells and reservoirs around fractures, resulting in the aggravation of hydrate decomposition and a more pronounced drop in reservoir temperature. On the other hand, the rapid decomposition of hydrate increases gas production rapidly, enhances the throttling expansion effect near the horizontal well, and increases the degree of the temperature drop. As shown in Figure 10a−c, the temperature in the fracture is slightly higher than that in the adjacent hydrate reservoirs. This is because the fracture penetrates the reservoir, so it is easy to obtain the energy supplement from the reservoir.

Figure 11 shows the spatial distribution characteristics of gas saturation in the NGH reservoir without MFHW at different times. In the unfractured condition, the high gas saturation area is mainly distributed around the horizontal well. At the same time, due to the rapid decomposition rate of hydrate in the lower part of the horizontal well, the gas distribution in the lower part of the horizontal well is larger than that in the upper part. Figure 12 shows the spatial distribution characteristics of gas saturation in the NGH reservoir with five vertical fractures at different times. Since the presence of fractures aggravates the degree of hydrate decomposition, the gas saturation of the reservoir in the fractured case is significantly higher than that in the unfractured case. At 60 days and 365 days, the gas saturation in fractures is lower than that in adjacent reservoirs, while at 1095 days, the gas saturation in fractures is slightly higher. This is because, in the early stage of exploitation, the hydrate decomposition area is mainly located near the horizontal wells and fractures. The large

https://doi.org/10.1021/acsomega.2c03667
ACS Omega 2022, 7, 35705−35719

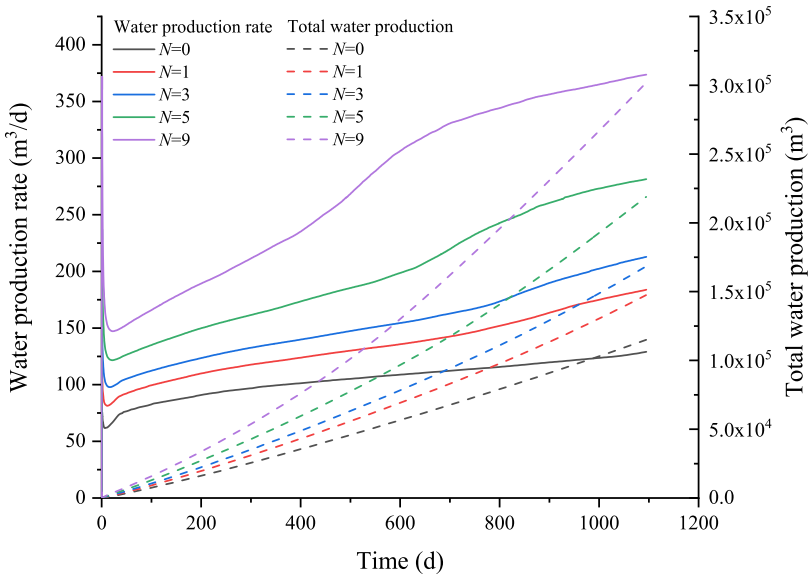

Figure 15. Evolution of the water production rate and total water production with time under different fracture numbers.

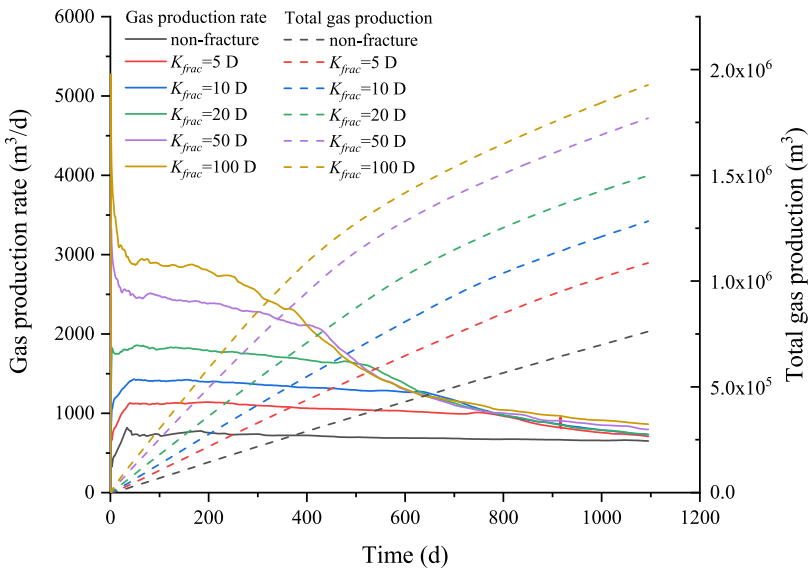

Figure 16. Evolution of the gas production rate and total gas production with time under different fracture permeabilities.

depressurization amplitude promotes rapid hydrate decomposition, resulting in high gas saturation in the reservoir. While the fractures with high conductivity enable the gas to flow into the production wells quickly, so the gas saturation in the fractures is low. In the later stage of production, the hydrate near the horizontal well and fracture is completely decomposed. The gas in the fracture is mainly from the areas far away from horizontal wells under the action of the pressure difference. The fracture with low pore pressure plays the role of gathering gas to cause a higher gas saturation.

3.2. Effect of the Fracture Number on Gas and Water Production. In this section, different vertical fracture numbers perpendicular to the axis are set at the same length of the horizontal well to predict the gas production rate and total gas production. Figure 13 shows the evolution of the gas production rate and total gas production with time under different fracture numbers. When the fracture numbers increase from 0 to 1, 3, 5, and 9, the peak gas production rate increases from 820 to 979, 1130, 1429, and 2042 m^3/d, with an increase of 19.39, 37.80, 74.27, and 149.02% respectively. The total gas production in 1095 days increased from 761 713 to 893 708, 1 058 200, 1 284 234, and 1 542 886 m^3, with an increase of 17.33, 38.92, 68.60, and 102.55%, respectively. The results show that setting one or three vertical fractures in a 40 m horizontal well can significantly increase the gas production, but the improvement effect is relatively limited; when the number of fractures increases to 5 or 9, the gas production increases significantly. The presence of fractures can effectively increase the contact area between the horizontal well and the NGH reservoir matrix and change the flow state in the low-permeability clayey silt hydrate reservoir. This makes the hydrate decomposition gas close to the fracture quickly flow into the horizontal well through the fracture. Thereby, the distance of the low-speed gas flow is shortened. The increase in the number of fractures allows a wider range of hydrate decomposition gas to flow rapidly into the fractures, resulting in a further improvement in productivity. The presence of fractures makes the gas production rate of hydrate reservoirs present different characteristics. When the

https://doi.org/10.1021/acsomega.2c03667
ACS Omega 2022, 7, 35705−35719

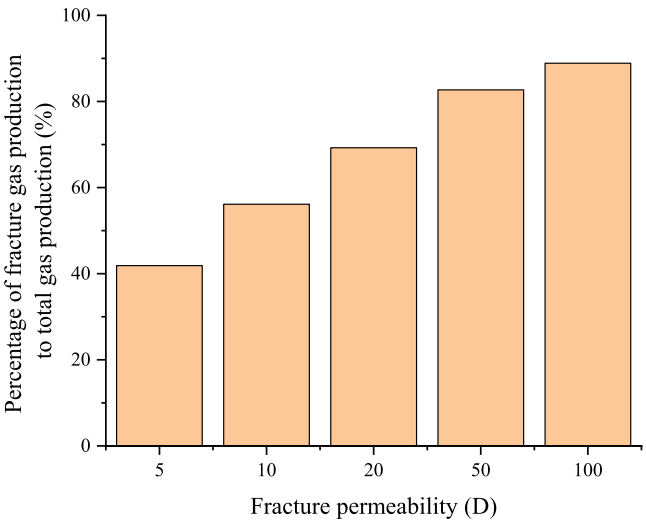

Figure 17. Percentage of gas production from fracture to total gas production under different fracture permeabilities.

number of fractures is 0, the gas production rate increases rapidly at first and then generally shows a slow downward trend. When the number of fractures is 1, 3, 5, and 9, the gas production rate increases rapidly first, then decreases slowly, and finally decreases faster. In the stage of the rapid increase of the gas production rate, the fluid around the well gradually flows to the production well, which continues to expand the depressurization range, resulting in the expansion of the hydrate decomposition range and the increase in gas production. In the high production stage, with a slow decline in the gas production rate, the gas production rate generally maintains a high level. However, as the front edge of hydrate decomposition gradually moves away from the fractures and production wells, the resistance along the flow of the hydrate decomposition gas increases, causing the gas production rate to decrease slowly. In the rapid decline stage, the gas production rate decreases rapidly due to the complete decomposition of interfracture hydrate. The increase in fracture numbers promotes the gas production rate in the high-yield stage. However, the greater gas production rate means that the hydrate between fractures decomposes faster, resulting in the complete decomposition of hydrate between fractures in a short time so that the gas production rate decreases rapidly in a relatively short time. Figure 14 indicates that when the number of fractures is 1, 3, 5, and 9, respectively, the percentage of gas production from fractures to the total gas production is 22.00, 37.40, 56.13, and 75.21%, respectively. Thus, the contribution of fractures to total gas production is gradually improved with the increase in the number of fractures.

Figure 15 shows the evolution of the water production rate and total water production with time under different fracture numbers. With the increase in fracture numbers, the water production rate in the fracturing cases is significantly higher than in the cases without fracture. The presence of fractures provides a high-speed flow channel for gas and water flow and increases the depressurization effect, thereby promoting hydrate decomposition. The effective permeability of the reservoir after hydrate decomposition is significantly improved, which further promotes water flow and increases water production. When the number of fractures is 9, 5, 3, and 1, the water production rate increases rapidly at 456, 630, 783, and 865 days, respectively, and more fractures make the water production rate increase more obvious. Hydrate decomposition in the upper and lower GHBL of horizontal wells weakens its self-sealing effect and promotes an increase in the water production rate. More fractures make the depressurization effect spread more effectively in the reservoir, which intensifies the rate of hydrate dissociation and promotes the weakening of the self-sealing effect of the hydrate layer and the rapid increase in the water production rate. The increase in the water production rate enhances the flow channels of water in the pore space and reduces the gas flow channel, which leads to the decrease of gas-phase effective permeability in the hydrate reservoir, resulting in a decrease in the gas production rate. In the third year, when the number of fractures increases from 0 to 1, 3, 5, and 9, the water production rate increases from 129 to 184, 213, 281, and 374 m^3/d, respectively, with an increase of 42.64, 65.12, 117.83, and 189.92% respectively. The total water production increases from 115 004 to 147 531, 168 507, 219 004, and 301 996 m^3,

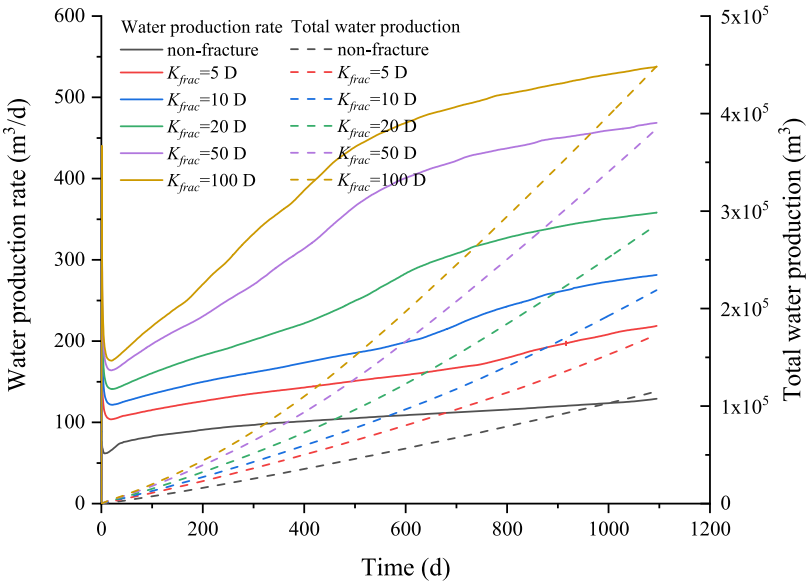

Figure 18. Evolution of the water production rate and total water production with time under different fracture numbers.

https://doi.org/10.1021/acsomega.2c03667
ACS Omega 2022, 7, 35705−35719

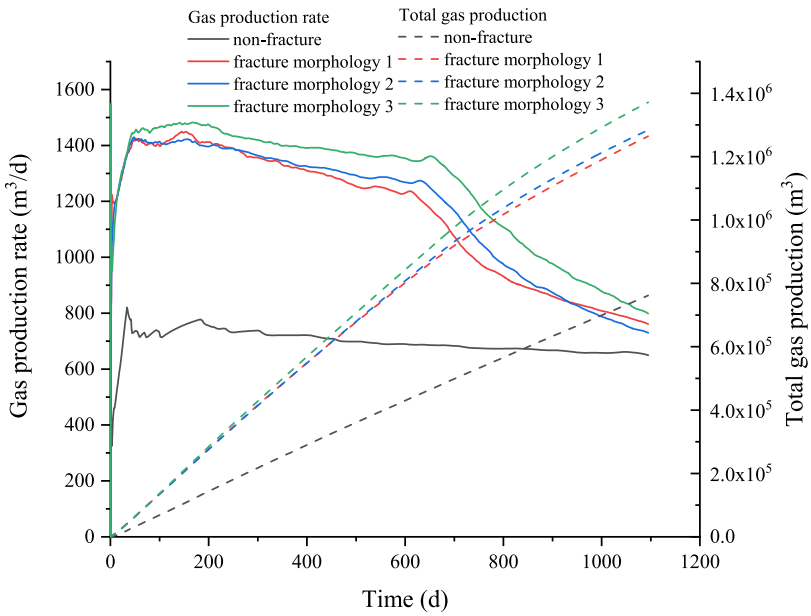

Figure 19. Evolution of the gas production rate and total gas production with time under different fracture morphologies.

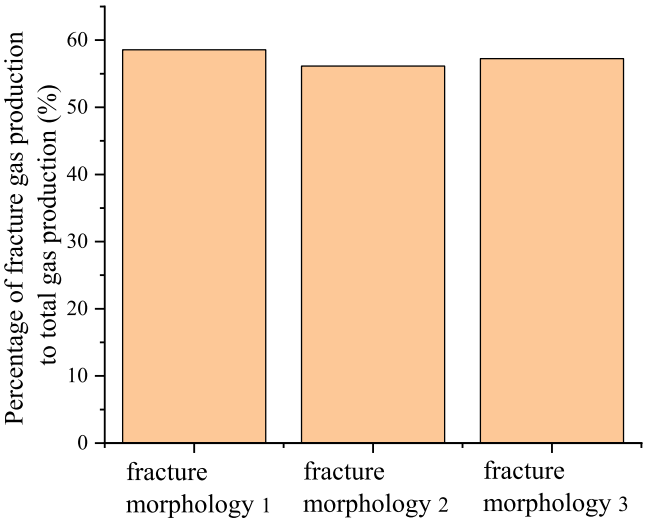

Figure 20. Percentage of fracture gas production to total gas production under different fracture morphologies.

respectively, with an increase of 28.28, 46.52, 90.43, and 162.60%, respectively.

3.3. Effect of Fracture Permeability on Gas and Water Production. In this section, five vertical fractures on the 40 m horizontal well section are set with different permeabilities. Figure 16 shows the evolution characteristics of the gas production rate and total gas production with time under different fracture permeabilities. When the fracture permeabilities are 5, 10, 20, 50, and 100 D, the peak gas production rates are 1131, 1429, 1859, 3333, and 5277 m^3/d, respectively, and the total gas production is 1 086 103, 1 284 234, 1 499 180, 1 770 196, and 1 927 450 m^3, respectively. Compared with the unfractured condition (761 713 m^3), the total gas production increased by 42.59, 68.60, 96.82, 132.40, and 153.04%, respectively. The larger fracture permeability means that the flow resistance of fluid in the fracture becomes smaller, which makes the fluid in the reservoir pores more easy to flow into the production well, thereby increasing the depressurization range, promoting hydrate decomposition, and improving gas production. As shown in Figure 17, when the fracture permeabilities are 5, 10, 20, 50, and 100 D, respectively, the percentages of fracture gas production to total gas production are 41.87, 56.13, 69.25, 82.70, 82.70, and 88.87%, respectively. With the increase in fracture permeability, the contribution of fracture gas production to total gas production increases. However, since the lower reservoir permeability limits the fluid supply capacity of the GHBL to fractures, when the permeability of fracture increases, the amplification in gas production gradually decreases. Overall, the stimulation effect of the hydrate reservoir is comprehensively affected by stratum fluid supply capacity and fracture permeability.

Figure 18 shows the evolution characteristics of the water production rate and total water production with time under different fracture permeabilities. At 1095 days, the water production rates with fracture permeabilities of 5, 10, 20, 50, and 100 D are 219, 281, 358, 469, and 538 m^3/d, respectively, and the total water production is 173 130, 219 004, 286 058, 384 450, and 448 524 m^3, respectively. Compared with the unfractured condition, the water production rate increased by 69.77, 117.83, 177.52, 263.57, and 317.05%, and the total water production increased by 50.54, 81.60, 148.74, 234.29, and 290.00%, respectively. This indicates that increasing the fracture permeability not only significantly increases gas production but also significantly enhances water production. Therefore, while considering the stimulation effect of fractures with high conductivity on the GHBL, it is also necessary to consider that the high water production rate makes it difficult for the electric submersible pump to deal with the problem of excessive water production so as to achieve the expected depressurization effect.

3.4. Effect of Fracture Morphology on Gas and Water Production. According to the previous simulation results, when the injection time of fracturing fluid is kept constant, increasing the injection rate of fracturing fluid increases the fracture area and changes the fracture morphology. Based on the previous numerical simulation results,[35] this section further studies the influence of different fracture morphologies on the

https://doi.org/10.1021/acsomega.2c03667
ACS Omega 2022, 7, 35705−35719

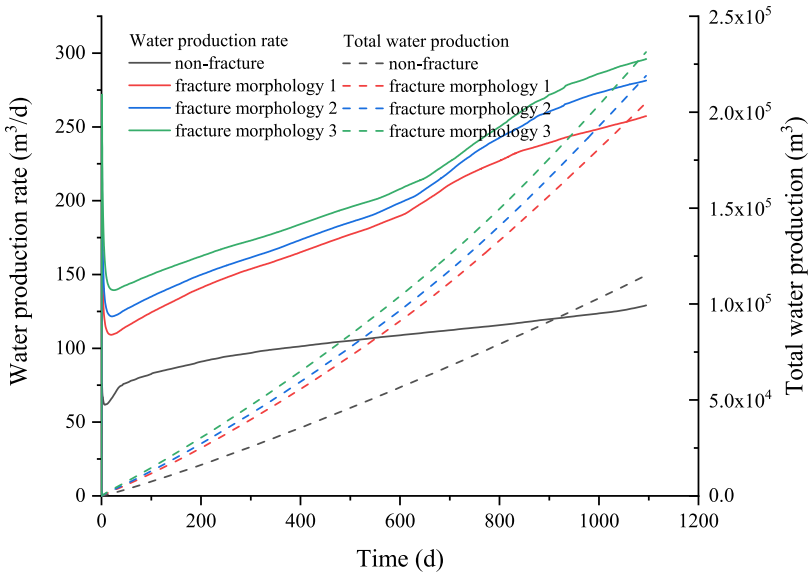

Figure 21. Evolution characteristics of the water production rate and total water production with time under different fracture forms.

stimulation effect. Fracture morphologies 1, 2, and 3, respectively, correspond to the fracture morphology extraction diagram under three different fracturing fluid injection rates shown in Figure 3. As shown in Figure 19, increasing the fracture area significantly promotes the gas production rate and total gas production. The total gas production of fracture morphologies 1, 2, and 3 is 1 264 878, 1 284 234, and 1 371 632 m^3, respectively. Compared with the unfractured case (761 713 m^3), the total gas production increases by 66.06, 68.60, and 80.07%, respectively. The increased fracture area enables rapid decomposition of hydrates far from the horizontal well, thus effectively improving the gas production rate and total gas production. At the same time, the larger fracture area increases the amount of hydrate between fractures, thereby increasing the duration of the high-yield stage. However, Figure 20 indicates that the contribution of fracture gas production to the total gas production does not increase significantly with the increase in the fracture area.

Figure 21 shows the evolution characteristics of the water production rate and total water production with time under different fracture forms. At the end of mining, the water production rates of fracture morphologies 1, 2, and 3 are 257, 281, and 296 m^3/d, respectively, and the total water production is 204 954, 219 004, and 231 410 m^3, respectively. This indicates that the increase in the fracture area will significantly promote the water production rate and total water production because a wider range of reservoir pore water and hydrate decomposition water can flow into production wells through fractures.

4. CONCLUSIONS

In this study, a three-dimensional numerical model was built to study the stimulation of MHFW technology on a clayey silt NGH reservoir. The effects of the fracture number, fracture permeability, and fracture morphology on gas production were studied. The main conclusions are as follows:

(1) The fractures generated by MFHW technology make the front edge of hydrate decomposition change from a radial distribution mode to the coexistence mode of radial and fracture propagation directions, which is due to the better depressurization effect produced by the fractures with high conductivity.

(2) Increasing the fracture number can effectively increase the contact area between the fractures and the NGH reservoir, thus making the gas production rate increase significantly. When the number of fractures increases from 1 to 5, the gas production increases from 17.33 to 102.55%.

(3) By reducing flow resistance, increasing fracture permeability effectively increases the depressurization range and gas production. When the fracture permeability increases from 2 to 100 D, the total gas production increases from 42.59 to 153.04%.

(4) The fracture morphology with a large fracture area can quickly decompose the hydrates far away from the production well, which effectively improves the gas production rate and total gas production. The total gas production of fracture morphologies 1, 2, and 3 increased by 66.06, 68.60, and 80.07%, respectively.

■ AUTHOR INFORMATION

Corresponding Authors

Xiaolong Ma − *State Key Laboratory of Geomechanics and Geotechnical Engineering, Institute of Rock and Soil Mechanics, Chinese Academy of Sciences, Wuhan 430000, China*; Email: maxiaolong0501@126.com

Dongbin Pan − *School of Resources and Environmental Engineering, Jiangxi University of Science and Technology, Ganzhou 341000, China*; Email: pandongbin@jxust.edu.cn

Author

Junpeng Han − *College of Construction Engineering, Jilin University, Changchun 130061, China*; orcid.org/0000-0002-1742-6089

Complete contact information is available at: https://pubs.acs.org/10.1021/acsomega.2c03667

Notes

The authors declare no competing financial interest.

https://doi.org/10.1021/acsomega.2c03667
ACS Omega 2022, 7, 35705−35719

ACKNOWLEDGMENTS

This study was supported by the National Natural Science Foundation of China (Grant No. 51991364) and the Science and technology research project of Jiangxi Provincial Department of Education (Grant No. GJJ210863).

REFERENCES

(1) Yin, Z.; Huang, L.; Linga, P. Effect of wellbore design on the production behaviour of methane hydrate-bearing sediments induced by depressurization. *Appl. Energy* **2019**, *254*, No. 113635.

(2) Sultaniya, A.; Priest, J. A.; Clayton, C. R. I. Impact of formation and dissociation conditions on stiffness of a hydrate-bearing sand. *Can. Geotech. J.* **2018**, *55*, 988−998.

(3) Boswell, R. C.; Timothy, S. Current perspectives on gas hydrate resources. *Energy Environ. Sci.* **2011**, *4*, 1206−1215.

(4) Chong, Z. R.; Yang, S. H. B.; Babu, P.; Linga, P.; Li, X. S. Review of natural gas hydrates as an energy resource: Prospects and challenges. *Appl. Energy* **2016**, *162*, 1633−1652.

(5) Fujii, T.; Suzuki, K.; Takayama, T.; Tamaki, M.; Komatsu, Y.; Konno, Y.; Yoneda, J.; Yamamoto, K.; Nagao, J. Geological setting and characterization of a methane hydrate reservoir distributed at the first offshore production test site on the Daini-Atsumi Knoll in the eastern Nankai Trough, Japan. *Mar. Pet. Geol.* **2015**, *66*, 310−322.

(6) Li, J.-f.; Ye, J.; Qin, X.; Qiu, H.; Wu, N.; et al. The first offshore natural gas hydrate production test in South China Sea. *China Geol.* **2018**, *1*, 5−16.

(7) Sun, Y.; Ma, X.; Guo, W.; Jia, R.; Li, B. Numerical simulation of the short- and long-term production behavior of the first offshore gas hydrate production test in the South China Sea. *J. Pet. Sci. Eng.* **2019**, *181*, No. 106196.

(8) Feng, Y.; Chen, L.; Suzuki, A.; Kogawa, T.; Okajima, J.; Komiya, A.; Maruyama, S. Numerical analysis of gas production from reservoir-scale methane hydrate by depressurization with a horizontal well: The effect of permeability anisotropy. *Mar. Pet. Geol.* **2019**, *102*, 817−828.

(9) Ma, X.; Sun, Y.; Liu, B.; Guo, W.; Li, S.; et al. Numerical study of depressurization and hot water injection for gas hydrate production in China's first offshore test site. *J. Nat. Gas Sci. Eng.* **2020**, *83*, No. 103530.

(10) Mao, P. X.; Wan, Y. Z.; Sun, J. X.; Li, Y. L.; Hu, G. W.; Ning, F. L.; Wu, N. Numerical study of gas production from fine-grained hydrate reservoirs using a multilateral horizontal well system. *Appl. Energy* **2021**, *301*, No. 117450.

(11) Yu, T.; Guan, G.; Abudula, A.; Wang, D. 3D investigation of the effects of multiple-well systems on methane hydrate production in a low-permeability reservoir. *J. Nat. Gas Sci. Eng.* **2020**, *76*, No. 103213.

(12) Ma, X.; Sun, Y.; Guo, W.; Jia, R.; Li, B. Numerical simulation of horizontal well hydraulic fracturing technology for gas production from hydrate reservoir. *Appl. Ocean Res.* **2021**, *112*, No. 102674.

(13) Ma, X.; Cheng, J.; Sun, Y.; Li, S. 2D Numerical Simulation of Hydraulic Fracturing in Hydrate-Bearing Sediments Based on the Cohesive Element. *Energy Fuels* **2021**, *35*, 3825−3840.

(14) Ye, J.; Qin, X.; Xie, W.; Lu, H.; Ma, B.; Qiu, H.; et al. Main progress of the second gas hydrate trial production in the South China Sea. *Geol. China* **2020**, *47*, 557−568.

(15) Li, B.; Ma, X.; Zhang, G.; Guo, W.; Xu, T.; Yuan, Y.; Sun, Y. Enhancement of gas production from natural gas hydrate reservoir by reservoir stimulation with the stratification split grouting foam mortar method. *J. Nat. Gas Sci. Eng.* **2020**, *81*, No. 103473.

(16) He, Y.; Qin, J.; Cheng, S.; Chen, J. Estimation of fracture production and water breakthrough locations of multi-stage fractured horizontal wells combining pressure-transient analysis and electrical resistance tomography. *J. Pet. Sci. Eng.* **2020**, *194*, No. 107479.

(17) Gao, D.; Liu, Y.; Pan, S.; Wang, J.; Zhou, X. Longitudinal interference analysis of shale gas multi-stage fracturing horizontal wells upon high-precision pressure test. *Energy Sci. Eng.* **2020**, *8*, 2387−2401.

(18) Wang, Z.; Zhang, L.; Zhang, R.; Wang, R.; Huang, R. Flow Mechanism and Transient Pressure Analysis of Multi-Stage Fractured Horizontal Well. *Chem. Technol. Fuels Oils* **2022**, *57*, 941−954.

(19) Zhang, H.; Sheng, J. Optimization of horizontal well fracturing in shale gas reservoir based on stimulated reservoir volume. *J. Pet. Sci. Eng.* **2020**, *190*, No. 107059.

(20) Xu, Y.; Li, X.; Liu, Q. Pressure performance of multi-stage fractured horizontal well with stimulated reservoir volume and irregular fractures distribution in shale gas reservoirs. *J. Nat. Gas Sci. Eng.* **2020**, *77*, No. 103209.

(21) Xie, W.; Li, X.; Zhang, L.; Wang, J.; Cao, L.; Yuan, L. Two-phase pressure transient analysis for multi-stage fractured horizontal well in shale gas reservoirs. *J. Nat. Gas Sci. Eng.* **2014**, *21*, 691−699.

(22) Li, D.; Wang, Y.; Zeng, B.; Lyu, Q.; Zhou, X.; Zhang, N. Optimization of the shale gas reservoir fracture parameters based on the fully coupled gas flow and effective stress model. *Energy Sci. Eng.* **2021**, *9*, 676−693.

(23) Cui, Y.; Jiang, R.; Wang, Q.; Liu, X. Production performance analysis of multi-fractured horizontal well in shale gas reservoir considering space variable and stress-sensitive fractures. *J. Pet. Sci. Eng.* **2021**, *207*, 109171.

(24) Zhao, J.; Xu, L.; Guo, X.; Li, Q.; Lv, X.; Fan, Q.; Zhao, J.; Dong, H.; Wang, B.; Yang, L. Enhancing the gas production efficiency of depressurization-induced methane hydrate exploitation via fracturing. *Fuel* **2021**, *288*, No. 119740.

(25) Ma, X.; Sun, Y.; Guo, W.; Jia, R.; Li, B. Numerical simulation of horizontal well hydraulic fracturing technology for gas production from hydrate reservoir. *Appl. Ocean Res.* **2021**, *112*, No. 102674.

(26) Feng, Y.; Chen, L.; Suzuki, A.; Kogawa, T.; Okajima, J.; Komiya, A.; Maruyama, S. Enhancement of gas production from methane hydrate reservoirs by the combination of hydraulic fracturing and depressurization method. *Energy Convers. Manage.* **2019**, *184*, 194−204.

(27) Moridis, G. J.; Kowalsky, M. B.; Pruess, K. *TOUGH+HYDRATE V1. 0 User's Manual: a Code for the Simulation of System Behavior in Hydrate-bearing Geologic Media*, 2008.

(28) Moridis, G. J. *User's Manual for the Hydrate v1.5 Option of TOUGH+ v1.5: A Code for the Simulation of System Behavior in Hydrate-Bearing Geologic Media*, 2014.

(29) Li, B.; Li, X-S.; Li, G.; Feng, J.-C.; Wang, Y. Depressurization induced gas production from hydrate deposits with low gas saturation in a pilot-scale hydrate simulator. *Appl. Energy* **2014**, *129*, 274−286.

(30) Yin, Z.; Moridis, G.; Chong, Z. R.; Tan, H. K.; Linga, P. Numerical analysis of experimental studies of methane hydrate dissociation induced by depressurization in a sandy porous medium. *Appl. Energy* **2018**, *230*, 444−459.

(31) Yin, Z.; Moridis, G.; Tan, H. K.; Linga, P. Numerical analysis of experimental studies of methane hydrate formation in a sandy porous medium. *Appl. Energy* **2018**, *220*, 681−704.

(32) Yu, T.; Guan, G.; Abudula, A. Production performance and numerical investigation of the 2017 offshore methane hydrate production test in the Nankai Trough of Japan. *Appl. Energy* **2019**, *251*, No. 113338.

(33) Chen, L.; Feng, Y.; Okajima, J.; Komiya, A.; Maruyama, S. Production behavior and numerical analysis for 2017 methane hydrate extraction test of Shenhu, South China Sea. *J. Nat. Gas Sci. Eng.* **2018**, *53*, 55−66.

(34) Li, G.; Moridis, G. J.; Zhang, K.; Li, X. S. Evaluation of Gas Production Potential from Marine Gas Hydrate Deposits in Shenhu Area of South China Sea. *Energy Fuels* **2010**, *24*, 6018−6033.

(35) Ma, X.; Jiang, D.; Fang, X.; Wang, X. Numerical simulation of single-cluster and multi-cluster fracturing of hydrate reservoir based on cohesive element. *Eng. Fract. Mech.* **2022**, *265*, 108365.

(36) Moridis, G. J.; Reagan, M. T. Estimating the upper limit of gas production from Class 2 hydrate accumulations in the permafrost: 1. Concepts, system description, and the production base case. *J. Pet. Sci. Eng.* **2011**, *76*, 194−204.

(37) Zhang, R. H.; Zhang, L. H.; Tang, H. Y.; Chen, S. N.; Zhao, Y. L.; Wu, J. F.; Wang, K. R. A simulator for production prediction of multistage fractured horizontal well in shale gas reservoir considering complex fracture geometry. *J. Nat. Gas Sci. Eng.* **2019**, *67*, 14−29.

https://doi.org/10.1021/acsomega.2c03667
ACS Omega 2022, 7, 35705−35719

(38) Li, X. S.; Yang, B.; Li, G.; Li, B. Numerical Simulation of Gas Production from Natural Gas Hydrate Using a Single Horizontal Well by Depressurization in Qilian Mountain Permafrost. *Ind. Eng. Chem. Res.* **2012**, *51*, 4424−4432.
(39) Li, X. S.; Li, B.; Li, G.; Yang, B. Numerical simulation of gas production potential from permafrost hydrate deposits by huff and puff method in a single horizontal well in Qilian Mountain, Qinghai province. *Energy* **2012**, *40*, 59−75.
(40) Su, Z.; Moridis, G. J.; Zhang, K.; Wu, N. A huff-and-puff production of gas hydrate deposits in Shenhu area of South China Sea through a vertical well. *J. Pet. Sci. Eng.* **2012**, *86-87*, 54−61.
(41) Jin, G.; Xu, T.; Xin, X.; Wei, M.; Liu, C. Numerical evaluation of the methane production from unconfined gas hydrate-bearing sediment by thermal stimulation and depressurization in Shenhu area, South China Sea. *J. Nat. Gas Sci. Eng.* **2016**, *33*, 497−508.
(42) Sun, J.; Ning, F.; Liu, T.; Liu, C.; Chen, Q.; Li, Y.; Cao, X.; Mao, P.; Zhang, L.; Jiang, G. Gas production from a silty hydrate reservoir in the South China Sea using hydraulic fracturing: A numerical simulation. *Energy Sci. Eng.* **2019**, *7*, 1106−1122.
(43) Rutqvist, J.; Moridis, G. J.; Grover, T.; Collett, T. Geomechanical response of permafrost-associated hydrate deposits to depressurization-induced gas production. *J. Pet. Sci. Eng.* **2009**, *67*, 1−12.
(44) Moridis, G. J.; Kowalsky, M. B. Response of oceanic hydrate-bearing sediments to thermal stresses. *SPE J.* **2007**, *12*, 253−268.
(45) Yu, T.; Guan, G.; Abudula, A.; Yoshida, A.; Wang, D.; Song, Y. Heat-assisted production strategy for oceanic methane hydrate development in the Nankai Trough, Japan. *J. Pet. Sci. Eng.* **2019**, *174*, 649−662.
(46) Su, Z.; Huang, L.; Wu, N. Y.; Yang, S. X. Effect of thermal stimulation on gas production from hydrate deposits in Shenhu area of the South China Sea. *Sci. China Earth Sci.* **2013**, *56*, 601−610.

https://doi.org/10.1021/acsomega.2c03667
ACS Omega 2022, 7, 35705−35719